PROCEEDINGS OF SPIE

SPIEDigitalLibrary.org/conference-proceedings-of-spie

A retinal-projection-based near-eye display with contact lens for mixed reality

Wenbo Zhang, Chao Ping Chen, Lantian Mi, Yifan Lu, Ming Zhu, et al.

Wenbo Zhang, Chao Ping Chen, Lantian Mi, Yifan Lu, Ming Zhu, Xingyu Ren, Ruixue Tang, Nizamuddin Maitlo, "A retinal-projection-based near-eye display with contact lens for mixed reality," Proc. SPIE 11040, Optical Design Challenge 2019, 1104005 (27 February 2019); doi: 10.1117/12.2523452

SPIE.

Event: SPIE Optical Design Challenge, 2019, San Francisco, California, United States

A retinal-projection-based near-eye display with contact lens for mixed reality

Wenbo Zhang, Chao Ping Chen*, Lantian Mi, Yifan Lu, Ming Zhu, Xingyu Ren, Ruixue Tang, and Nizamuddin Maitlo
Smart Display Lab, Department of Electronic Engineering, Shanghai Jiao Tong University, Shanghai, China
*Corresponding author: ccp@sjtu.edu.cn

ABSTRACT

We propose a design of a retinal-projection-based near-eye display for achieving ultra-large field of view, vision correction, and occlusion. Our solution is highlighted by a contact lens combo, a transparent organic light-emitting diode panel, and a twisted nematic liquid crystal panel. Its design rules are set forth in detail, followed by the results and discussion regarding the field of view, angular resolution, modulation transfer function, contrast ratio, distortion, and simulated imaging.

Keywords: mixed reality, near-eye display, head-mounted display, contact lens, retinal projection, ultra-large field of view, vision correction, occlusion

1. INTRODUCTION

In recent years, the notion of mixed reality (MR) [1] has been going viral thanks to the staggering venture investments and countless media hypes. With MR, users are able to view the real world overlaid with computer-generated imagery and information. Such user experience can be realized by two types of optical solutions, i.e. video see-through displays and optical see-through near-eye displays (NEDs) [2]. The former is usually deployed on well-established mobile devices such as smartphones and tablets, while the latter on the immature wearable devices, *e.g.* smart glasses or headsets. As far as user experience is concerned, optical see-through NEDs outperform video see-through displays in that what you see is what you get. But sadly, an ideal solution for optical see-through NEDs that could perfectly live up to the requirements of MR is still a big challenge. For example, combiner-based NEDs—including beam splitters [3], semi-reflective mirrors [4], and holographic reflectors [5]—are often bulky and heavy if designed for a large field of view (FOV). Waveguide-based NEDs—including both planar [6] and freeform [7] waveguides—are more compact in terms of form factor as the optical path can be compressed into the waveguide. However, once the light enters into a waveguide, the maximum angle, at which it could leave, will be bound by the total internal reflection and the ways of out-coupling. Retinal-projection-based or direct-view NEDs—including retinal scanning [8], pinlight [9], and iOptik [10], in which the image is directly projected on the retina—may have both compactness and large FOVs, and yet each one has its own issues. The retinal scanning is vulnerable to the rotation of eyeball. The pinlight struggles with the change in the gaze direction, pupil size, and eye's focal state. The iOptik—a proprietary technology of Innovega—is identified as a contact lens embedded with a polarizer and a zone plate. Despite years of development, the viability of such contact lens remains unclear.

Unlike video see-through displays, optical see-through NEDs are of wearable devices. Therefore, optics aside, ergonomics merits special care as well. One of the ergonomic pain points to solve is to save the visually impaired users from the trouble of wearing extra eyeglasses. As earlier attempts, we introduced combiner-based [11-13], waveguide-based [14-16], and retinal-projection-based NEDs [17-19], which are merged with the prescription or corrective lenses for vision correction. In this paper, we shall extend to a different scenario when a subset of population would prefer to wear contact lens in the hope of yielding a better performance in outdoor activities. To satisfy this niche, a retinal-projection-based NED, which features a contact lens combo, a transparent organic light-emitting diode (OLED) panel, and a twisted nematic liquid crystal (TN-LC) panel, is proposed [20]. In what follows, its structure, design rules, and results and discussion are to be elaborated.

Optical Design Challenge 2019, edited by Bernard C. Kress, Christophe Peroz, Proc. of SPIE
Vol. 11040, 1104005 · © 2019 SPIE · CCC code: 0277-786X/19/$18 · doi: 10.1117/12.2523452

2. DESIGN PRINCIPLE

2.1 Proposed structure

Fig. 1 is a schematic drawing of the proposed NED, which involves four major components, *i.e.* an OLED panel, a TN-LC panel, a contact lens combo—including a contact lens, a patterned analyzer, and a microlens—and an eye. The OLED panel is supposed to be transparent and responsible for delivering the virtual images. To the inner side of the OLED panel is attached a polarizer that is vertically polarized. The TN-LC panel is capable of switching the polarization. The contact lens is tailored to correct the refractive anomalies of the eye. On top of the contact lens is coated a patterned analyzer, whose transmission axis (TA) at the inner part is same as that of polarizer but at the outer part orthogonal to the former, as shown in the inset of Fig. 1, where the blue double arrows denote TAs. On top of the inner part of analyzer is laminated a microlens, which is used to converge the light of OLED. L is the diagonal dimension of active area of OLED panel. D is the distance between the OLED panel and eye. R_i is the radius of inner part of patterned analyzer.

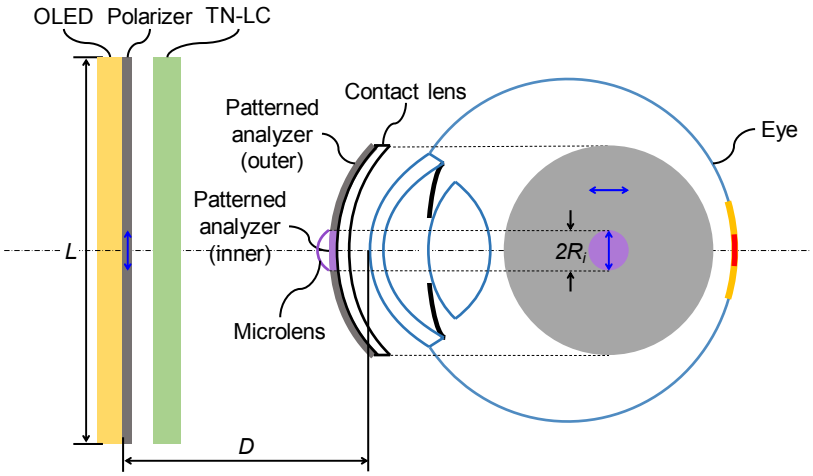

Fig. 1. Schematic drawing of the proposed NED, which involves four major components, *i.e.* an OLED panel, a TN-LC panel, a contact lens combo—including a contact lens, a patterned analyzer, and a microlens—and an eye.

2.2 Design rules

The design of the proposed NED deals with two optical paths, one for imaging the real object and the other for imaging the virtual object. The optical path diagrams for the real and virtual images are illustrated in Fig. 2 and Fig. 3, respectively. In imaging the real object, both OLED and TN-LC are turned off. As shown in Fig. 2, light rays emitting from the real object will first become vertically polarized after passing through the polarizer. When light is incident on the off-state TN-LC, a phenomenon known as optical activity is incurred [21], for which, the polarization of light at the exit will be rotated by 90°—*i.e.* horizontally polarized if viewed head-on. When rays reach the inner part of analyzer—which is vertically polarized—they will be blocked, implying that brightness of real image heavily leans on the size of inner part of analyzer. Only when rays reach the outer part of analyzer—which is horizontally polarized—they could be transmitted and then refracted in turn by the contact lens, cornea, and lens. Finally, an inverted image will be formed on the retina. The design of contact lens shall follow from the lensmaker's equation [21], as given by Eq. (1)

$$P_c = (n_c - 1)\left[\frac{1}{R_{cf}} - \frac{1}{R_{cb}}\right] \tag{1}$$

where P_c is diopter or optical power of contact lens, which can be obtained directly from the prescription, n_c is the refractive index of contact lens, R_{cf} and R_{cb} are the radii of curvature of the front and back surfaces of contact lens, respectively. The object distance s and image distance s' could be correlated as [20]

$$s = \frac{s'}{(P_e n_h + P_c)s' - n_h} \tag{2}$$

where P_e is diopter of eye, and n_h is the refractive index of vitreous humor. In practice, image distance s' shall be fixed to be equal to the length of eye ball, which is about 24-25 mm for an adult [22].

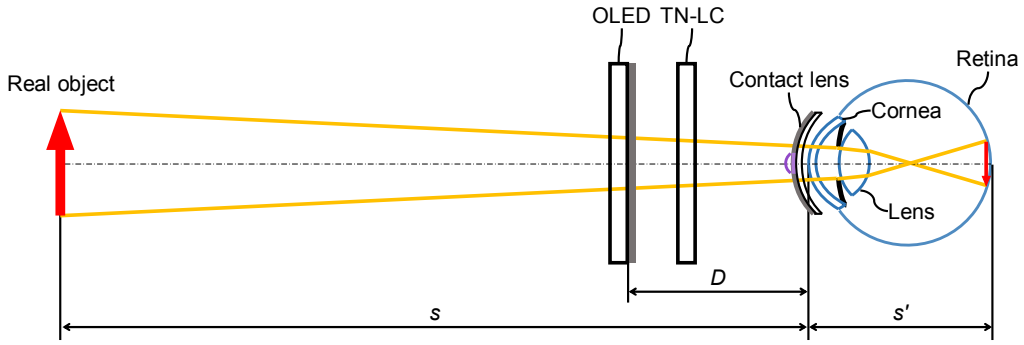

Fig. 2. Optical path diagram for imaging the real image, for which both OLED and TN-LC are turned off.

In imaging the virtual object, both OLED and TN-LC are turned on. As shown in Fig. 3, light rays emitting from the virtual object—*i.e.* the screen of OLED—will first become vertically polarized after passing through the polarizer. When incident on the on-state TN-LC, the optical activity is deactivated, for which, the polarization of light at the exit will remain unchanged. When rays reach the outer part of analyzer, they will be blocked. On the other hand, when rays reach the inner part of analyzer, they could be transmitted. This arrangement of patterned analyzer guarantees that when viewing the virtual object, no rays from the real object would stand in the way. This is particularly important for the outdoor usage as the strong ambient light would easily overwhelm the virtual object. Now the table could be turned for the ambient light will be substantially dampened by the patterned analyzer and even outshined by the OLED. In other words, the occlusion [2] between the real and virtual objects is enabled. Considering that OLED is too close to the eye that it is out of the range of accommodation, a microlens to pre-converge the rays is required to compensate the upper limit of range of accommodation. Again, employing lensmaker's equation, the diopter of microlens P_m is determined by

$$P_m = (n_m - 1)\left[\frac{1}{R_{mf}} - \frac{1}{R_{mb}}\right] \tag{3}$$

where n_m is the refractive index of microlens, R_{mf} and R_{mb} are the radii of curvature of the front and back surfaces of microlens, respectively. By intention, we let $R_{mb} = R_{cf}$ so that the diopter of analyzer is zero. Upon leaving the microlens and analyzer, rays are in turn refracted by the contact lens, cornea, and lens. Likewise, an inverted image will be formed on the retina. By factoring into P_m, Eq. (2) shall be modified as

$$s = \frac{s'}{(P_e n_h + P_c + P_m)s' - n_h} \tag{4}$$

from which, it can be seen that the presence of P_m shortens the object distance s that is identical to the distance D between the OLED panel and eye. Plus, the diopter of eye P_e may vary during the accommodation, in order for s' to be maintained on the retina so that sharp image can be formed, D could be manually adjusted. In fact, once the distance of real object exceeds 3 m, P_e will not change very much [20]. More importantly, although the physical distances of real and virtual objects—calculated by Eqs. (2) and (4)—are different, the psychological distances of real and virtual objects—processed by brain—will be equalized, as the depth cue of virtual object tends to be coupled with that of real object [23].

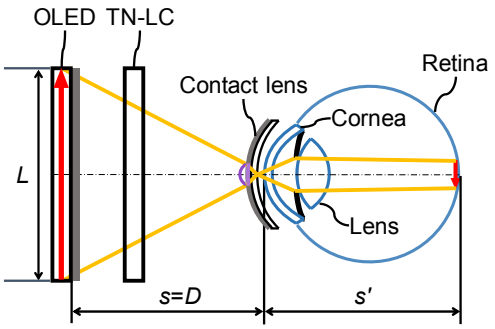

Fig. 3. Optical path diagram for imaging the virtual image, for which both OLED and TN-LC are turned on.

2.3 Contact lens combo

The contact lens combo consists of a contact lens, a patterned analyzer, and a microlens. The positions of contact lens and patterned analyzer are interchangeable. The microlens, patterned analyzer and contact lens are center-aligned. Patterned analyzer can be fashioned via the photoalignment technique [24]. Consider a case that a user has 3 diopters of myopia, disregarding the astigmatism and other types of refractive anomalies. Per the said design rules, a contact lens combo can be tentatively designed using the parameters as given in Table 1. It should be mentioned that those parameters are subject to change after the optimization, as will be done later. Incidentally, for the fact that contact lens is a medical device, it is highly recommended to resort to an optometrist or ophthalmologist for professional advice on whether is suitable or not to wear contact lens, frequency of use, choice of materials, water content, oxygen permeability etc.

Table 1. Parameters for the contact lens combo.

Object	Parameter	Value
Contact lens	P_c	$-3.34\ \mathrm{m}^{-1}$
	n_c@543 nm	1.4040
	R_{cf}	8.2460 mm
	R_{cb}	7.7200 mm
Patterned analyzer	R_i	0.45 mm
Microlens	P_m	$65.01\ \mathrm{m}^{-1}$
	n_m@543 nm	1.7543
	R_{mf}	4.8203 mm
	R_{mb}	8.2460 mm

2.4 OLED panel

OLED panel [25], acting as a virtual object, consists of an OLED and a polarizer. For the real image, it is switched off, whereas for the virtual image, it is switched on. Preferably, it is supposed to be highly transparent to enhance the light utilization. Alternatively, OLEDs can be replaced by the quantum dot light-emitting diodes [26] or other types of transparent displays. Due to the unavailability of transparent OLEDs of merely a couple of inches, a set of customized parameters are listed in Table 2, where the resolution is 1024×768 (XGA), diagonal is 1.7 inch, pixel size is 33.73 μm, transmittance of OLED is 30%, contrast ratio (CR) is 10000, transmittance of polarizer is 49%. The overall transmittance or transparency of OLED panel is 14.7%. For a better transparency, the resolution has to be reduced so as to increase the aperture ratio, meaning that there is a tradeoff between the transparency and resolution.

Table 2. Parameters for OLED panel.

Object	Parameter	Value
OLED	*Resolution*	1024×768 (XGA)
	L (diagonal)	1.7 inch (43.18 mm)
	W (horizontal)	34.54 mm
	H (vertical)	25.91 mm
	Pixel size	33.73 μm
	Transmittance	30%
	CR	10000
Polarizer	*Transmittance*	49%

2.5 TN-LC panel

TN-LC panel, acting as a polarization rotator, consists of a TN-LC [27], which is sandwiched between two glass substrates coated with indium tin oxide (ITO) electrodes and polyimide (PI) alignment layers, as shown in Fig. 4. The switching of TN-LC should be synchronized with OLED. In the off-state—null voltage is applied—LC directors at the entrance and exit are perpendicular to one another. Under such configuration, the polarization of emerging light will be rotated by 90° via the optical activity [27]. In the on-state—a voltage is applied—the twist of LC directors is unwound, thereby lifting the optical activity. As a result, the polarization of emerging light will remain intact. To fulfill the first maximum of Mauguin condition [27], cellgap of LC layer d_{lc}, birefringence of LC Δn, and wavelength λ shall meet

$$d_{lc} = \frac{\sqrt{3}\lambda}{2\Delta n} \tag{5}$$

Say Δn= 0.1 (n_o= 1.49, n_e= 1.59) and λ= 543 nm, d_{lc}= 4.7 μm. Though Mauguin condition can be fulfilled at greater maximums, thicker cellgap of LC layer will definitely slow down the switching of TN-LC [27]. Since Mauguin condition is wavelength sensitive, the polarization rotation will not be perfect for the entire spectrum. As shown in Fig. 5, wavelength-dependent transmittance of off-state TN-LC panel can be computed with Jones matrix method [28]. Deviating from the design wavelength (543 nm), a loss of transmittance of up to 9% would translate into an imperfect occlusion between the real and virtual objects.

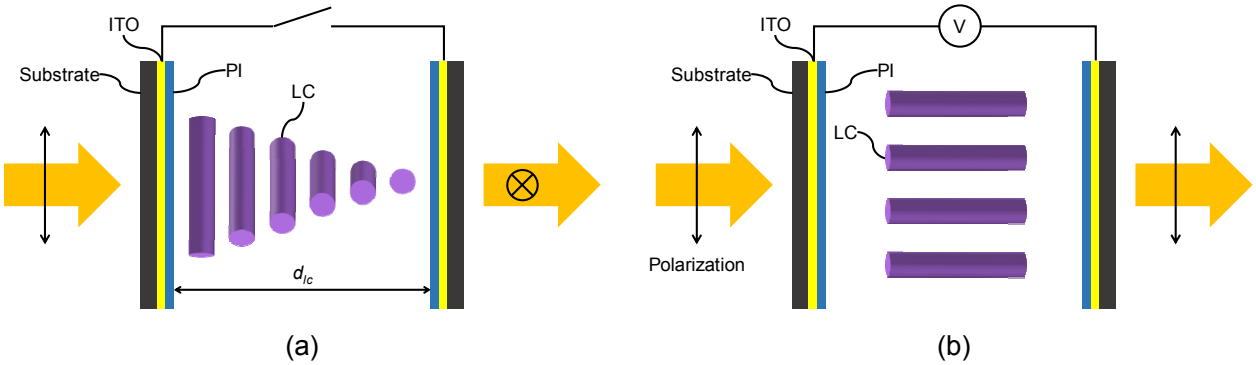

Fig. 4. Polarization switching of TN-LC panel. In the (a) off-state—null voltage is applied—LC directors at the entrance and exit are perpendicular to one another. Under such configuration, the polarization of emerging light will be rotated by 90° via the optical activity. In the (b) on-state—a voltage is applied—the twist of LC directors is unwound, thereby lifting the optical activity. As a result, the polarization of emerging light will remain intact.

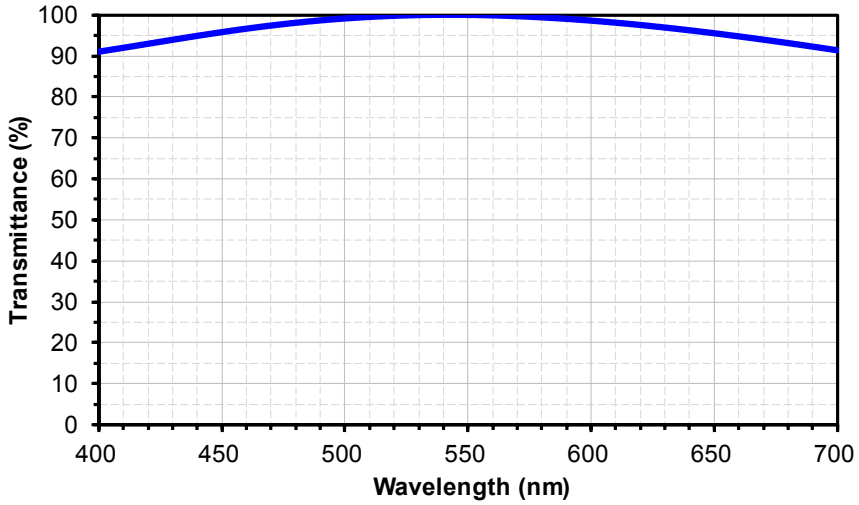

Fig. 5. Wavelength-dependent transmittance of off-state TN-LC panel. Since Mauguin condition is wavelength sensitive, the polarization rotation will not be perfect for the entire spectrum. Deviating from the design wavelength (543 nm), a loss of transmittance of up to 9% would translate into an imperfect occlusion between the real and virtual objects.

3. RESULTS AND DISCUSSION

3.1 Simulation settings

Our simulation is implemented with an optical design software Code V (Synopsys), which is based on the ray tracing [29] and capable of analyzing the imaging properties, including modulation transfer function (MTF), distortion, and imaging simulation. The design wavelengths are 458, 543, and 632.8 nm. The fields of 0° (center of fovea) and 9° (periphery of macula), and 55° are selected. As OLED, polarizer, TN-LC, and patterned analyzer are free of diopters, they are omitted during the calculation of imaging properties.

The numbering of surfaces is labeled as in Fig. 6. The real and virtual objects are situated at 3 m and 15 mm away from the eye, respectively. Surfaces 1 to 2 (S1 to S2) make up the microlens. Surfaces 2 to 3 (S2 to S3) make up the contact lens. Surfaces 3 to 8 (S3 to S8) make up the eye, of which, S3 is anterior cornea, S4 posterior cornea, S5 pupil, S6 anterior lens, S7 posterior lens, and S8 retina. In calculating the real image, real object and surfaces from S2 to S8 are active, of which S5 is assigned as stop. In calculating the virtual image, virtual object and surfaces from S1 to S8 are active, of which S2 is assigned as stop.

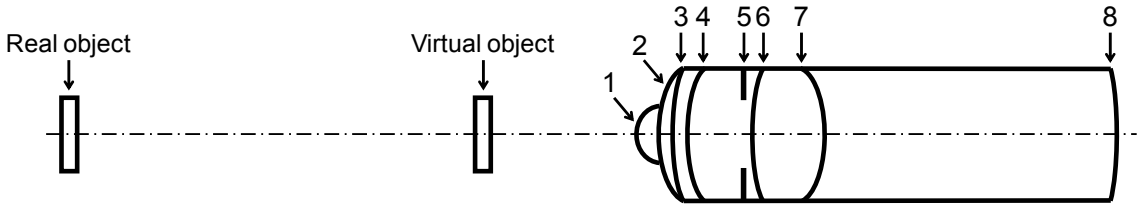

Fig. 6. Numbering of surfaces. The real and virtual objects are situated at 3 m and 15 mm away from the eye, respectively. Surfaces 1 to 2 (S1 to S2) make up the microlens. Surfaces 2 to 3 (S2 to S3) make up the contact lens. Surfaces 3 to 8 (S3 to S8) make up the eye, of which, S3 is anterior cornea, S4 posterior cornea, S5 pupil, S6 anterior lens, S7 posterior lens, and S8 retina. In calculating the real image, real object and surfaces from S2 to S8 are active. In calculating the virtual image, virtual object and surfaces from S1 to S8 are active.

To model the eye, the structural parameters of eye are originally adopted from a schematic eye proposed by Navarro *et al.* [30]. Along with the preliminary parameters enumerated in the previous section, we could build an initial NED design by presetting the surfaces of each element. Two optimizations are carried out in turn for the real and virtual images. At first, an optimization for the real image is done by constraining the length of the eye to be 24 mm. Then, fixing the as-optimized parameters for eye and contact lens, an optimization for the virtual image is done by tweaking the microlens only. The final parameters obtained after the optimization are summarized in Table 3. Besides, more detailed parameters for defining aspherical surfaces are disclosed in Table 4.

Table 3. Parameters used for the simulation.

Surface	Surface type	Radius (mm)	Thickness (mm)	Refractive index[a]@458 / 543 / 632.8 nm	Semi-aperture[b] (mm)
real/virtual object	sphere	infinity	3000 / 15[c]		
1 (microlens)	asphere	4.8203	0.0500	1.7600 / 1.7543 / 1.7440	N/A / 0.4734
2 (contact lens)	asphere	8.2460	0.0800	1.4140 / 1.4040 / 1.3940	4.3392 / 0.4500
3 (anterior cornea)	asphere	7.7200	0.5500	1.3828 / 1.3777 / 1.3747	4.5146 / 0.5037
4 (posterior cornea)	asphere	6.5000	2.4262	1.3445 / 1.3391 / 1.3360	4.2429 / 0.8950
5 (pupil)	sphere	infinity	0.0000	1.3445 / 1.3391 / 1.3360	2.5203
6 (anterior lens)	asphere	9.7368	4.6291	1.4292 / 1.4222 / 1.4183	3.1017 / 3.0390
7 (posterior lens)	asphere	-4.3341	16.3100	1.3428 / 1.3377 / 1.3347	4.0684 / 4.0551
8 (retina)	sphere	-12.0000	0.0000	1.3428 / 1.3377 / 1.3347	12.0000/ 11.1787

[a]Refractive indices are left empty when the medium is air. [b]Semi-apertures are given for calculating the real and virtual images, respectively. [c]Thicknesses of object are 3000 and 15 mm for calculating the real and virtual images, respectively.

Table 4. Parameters for aspherical surfaces.

Surface	Y radius (mm)	Conic constant (K)	4th order coefficient (A)	6th order coefficient (B)	8th order coefficient (C)
1 (microlens)	4.8203	57.7339	-0.0710	-0.0196	-0.4175
2 (contact lens)	8.2460	2.4278	-0.0013	1.4633E-05	8.5194E-07
3 (anterior cornea)	7.7200	-0.26	0	0	0
4 (posterior cornea)	6.5000	-2.0839	-0.0007	0	0
6 (anterior lens)	9.7368	2.8088	0.0008	0.0002	0
7 (posterior lens)	-4.3341	-0.8747	-0.0002	7.3075E-08	0

3.2 Field of view

Table 5 lists the parameters necessary for evaluating FOVs. Pursuant to the definitions of FOVs [20], FOV_r and FOV_v are calculated as 153° (diagonal) and 110° (diagonal), respectively.

Table 5. Parameters for calculating FOVs.

Object	Parameter	Value
FOV_r	Horizontal	150°
	Vertical	120°
FOV_v	*L*	1.7 inch (43.18 mm)
	D	15 mm

3.3 Angular resolution

Angular resolution—measured in arcminute (′)—of the image formed on the retina relies on both the resolutions of object and eye. For the resolution of real object is usually way higher than that of eye, angular resolution of the real image, AR_r, shall be equal to the latter, which is the reciprocal of visual acuity [31]. Thus,

$$AR_r = \frac{1}{visual\ acuity} \tag{6}$$

Under the best condition that the visual acuity is 1.0, angular resolution is 1′. For the resolution of OLED—defined as the average angular subtense of a single pixel—is usually way lower than that of eye, angular resolution of the virtual image, AR_v, on the contrary, shall be decided by the former, which can be calculated by dividing FOV_v by the number of pixels *N* along the diagonal, expressed as

$$AR_v = \frac{60 \cdot FOV_v}{N} = \frac{60 \cdot FOV_v}{\sqrt{N_h^2 + N_v^2}} \tag{7}$$

where N_h and N_v are the number of pixels along the horizontal and vertical directions, respectively. For FOV_v= 110°, N_h = 1024, and N_v = 768, angular resolution 5.16′. To reach the visual limit of 1′, a much higher resolution up to 7680×4320—*i.e.* 8K ultra-high-definition—will suffice, for which the angular resolution is as fine as 0.75′. It also should be cautioned that the above definition for AR_v will no longer hold once the resolution of OLED is better than 2′, if it is legitimate to think of the imaging of eye as a sampling process [32].

3.4 Modulation transfer function

By computing the auto-correlation of the pupil function [33], diffraction MTFs of both real and virtual images are calculated as a function of spatial frequency—the number of cycles or line pairs per millimeter—for the diffraction limit and fields of 0°, 9° and 55° (tangential and radial), as shown in Fig. 7. For the real image, MTFs within the macula are above 0.4 at 6 cycles/mm. For the virtual image, MTFs within the macula are above 0.4 at 20 cycles/mm.

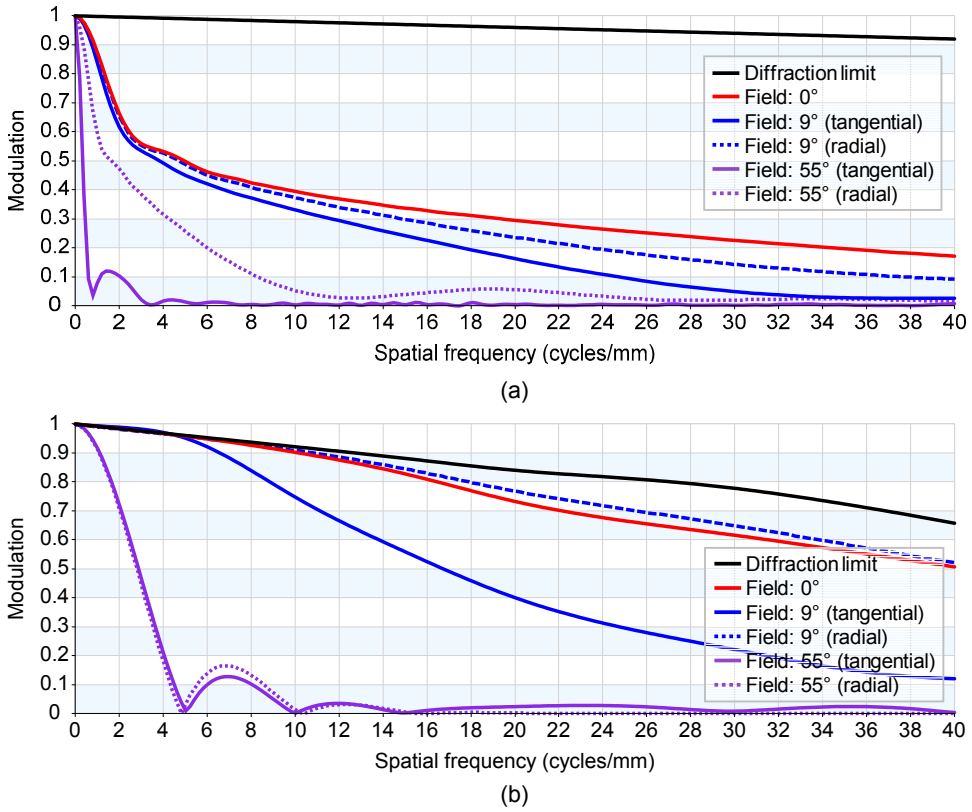

Fig. 7. Calculated MTFs of (a) real and (b) virtual images. For the real image, MTFs within the macula are above 0.4 at 6 cycles/mm. For the virtual image, MTFs within the macula are above 0.4 at 20 cycles/mm.

3.5 Contrast ratio

Contrast ratio—if treated as a transient quantity—is defined as the ratio of maximum intensity to minimum intensity [29], and it can be derived as [17]

$$CR = \frac{1+M\cdot MTF}{1-M\cdot MTF} \tag{8}$$

where M denotes the modulation in object, *i.e.*

$$M = \frac{CR_o-1}{CR_o+1} \tag{9}$$

where CR_o is the CR of object. For the real object, CR_o can be infinitely large so that M is deemed as 1. For the virtual object, CR_o is the CR of OLED. Since the real and virtual objects are situated at different distances, for an apples-to-apples comparison, the foregoing spatial frequency shall be converted to the number of cycles per degree. For the field of 0° at a spatial frequency of 3.89 cycles/degree—which corresponds to a pixel size of 33.73 μm at a distance of 15 mm—CRs of real and virtual images are calculated as 1999 (MTF= 0.999) and 11 (MTF= 0.827), respectively. By the way, the influence of TN-LC panel on the CR can be neglected, as it would diminish the maximum and minimum intensities of both real and virtual objects in proportion.

3.6 Distortion

Distortions of real and virtual images, defined as the displacement of image height or ray location, are plotted in Fig. 8, where the distortions of real and virtual images are less than 29% and 45%, respectively. Considering the fact that the distortion is an intrinsic property of eye [22], an absolutely distortion-free NED might not be very necessary. Instead, a certain distortion would be advantageous for the virtual world to be meshed perfectly with the real world, as long as the distortions of real and virtual images could be overlapped.

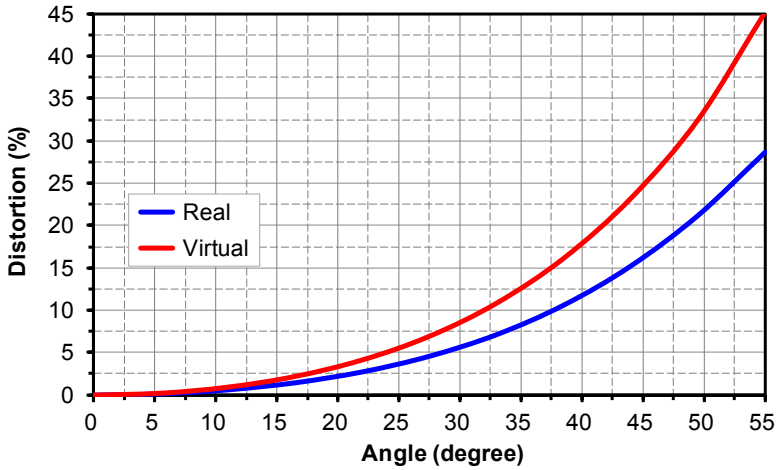

Fig. 8. Calculated distortions of real and virtual images. For real and virtual images, the distortions are less than 29% and 45%, respectively.

3.7 Simulated imaging

For a qualitative analysis of imaging quality, both real and virtual images are visualized from the imaging simulation that takes into account the effects of distortion, aberration blurring, diffraction blurring, and relative illumination, as shown in Fig. 9. By comparing the original and simulated images, it can be seen that the real image is inherently distorted at large field angles, while the virtual image turns out to be more blurred and more pronounced in the chromatic aberration. It has to be mentioned that those simulated images are what appear on the retina.

(a) (b) (c)

Fig. 9. (a) Original (photographer: C. P. Chen, location: Flaming Mountains, Turpan, China), (b) real, and (c) virtual images. By comparing the original and simulated images, it can be seen that the real image is inherently distorted at large field angles, while the virtual image turns out to be more blurred and more pronounced in the chromatic aberration.

4. CONCLUSIONS

A retinal-projection-based NED and design rules thereof are proposed. Its structure is characterized by a contact lens combo, a transparent OLED panel, and a TN-LC panel. Based on the simulation, its key performance including FOV, angular resolution, MTF, CR, and distortion has been studied. For the real image, FOV is 153° (diagonal), angular resolution is 1′, MTF is above 0.4 at 6 cycles/mm, CR is 1999, and the distortion is less than 29%. For the virtual image, FOV is 110° (diagonal), angular resolution is 5.16′, MTF is above 0.4 at 20 cycles/mm, CR is 11, and the distortion is less than 45%. Targeting the niche market on the contact-lens-wearing users and outdoor MR applications, our solution would offer several technical edges or possibilities that might be difficult with the current practices. First, its ultra-large FOVs for both real and virtual images are unparalleled by the others. Second, as opposed to eyeglasses, contact lens combo saves more room. Moreover, similar to polarized sunglasses, the analyzer within the combo could block the ultraviolet light and mitigate the glare [34]. Third, apart from being an optical device, contact lens combo can even cater to cosmetic needs by tinting the non-optical area of lens. Fourth, the occlusion between real and virtual objects is achieved by the patterning of analyzer and polarization switching of TN-LC.

ACKNOWLEDGMENTS

This work is supported by National Natural Science Foundation of China (61831015); Science and Technology Commission of Shanghai Municipality (1801H163000, 1701H169200); Shanghai Rockers Inc. (15H100000157); Shanghai Jiao Tong University (AF0300204).

REFERENCES

[1] Wikipedia, "Mixed reality," https://en.wikipedia.org/wiki/Mixed_reality.
[2] W. Barfield, *Fundamentals of Wearable Computers and Augmented Reality 2nd Edition* (Chemical Rubber Company, 2015).
[3] G.-Y. Lee, J.-Y. Hong, S. Hwang, S. Moon, H. Kang, S. Jeon, H. Kim, J.-H. Jeong, and B. Lee, "Metasurface eyepiece for augmented reality," Nat. Commun. **9**, 4562 (2018).
[4] S. Liu, H. Hua, and D. Cheng, "A novel prototype for an optical see-through head-mounted display with addressable focus cues," IEEE Trans. Vis. Comput. Graph. **16**(3), 381–393 (2010).
[5] A. Maimone, A. Georgiou, and J. S. Kollin, "Holographic near-eye displays for virtual and augmented reality," ACM Trans. Graph. **36**(4), 85 (2017).
[6] T. Levola, "Diffractive optics for virtual reality displays," J. Soc. Inf. Disp. **14**(5), 467–475 (2006).
[7] X. Hu and H. Hua, "High-resolution optical see-through multi-focal-plane head-mounted display using freeform optics," Opt. Express **22**(11), 13896–13903 (2014).
[8] S. C. McQuaide, E. J. Seibel, J. P. Kelly, B. T. Schowengerdt, and T. A. Furness III, "A retinal scanning display system that produces multiple focal planes with a deformable membrane mirror," Displays **24**(2), 65–72 (2003).
[9] A. Maimone, D. Lanman, K. Rathinavel, K. Keller, D. Luebke, and H. Fuchs, "Pinlight displays: wide field of view augmented reality eyeglasses using defocused point light sources," ACM Trans. Graph. **33**(4), 89 (2014).
[10] R. Sprague, A. Zhang, L. Hendricks, T. O'Brien, J. Ford, E. Tremblay, and T. Rutherford, "Novel HMD concepts from the DARPA SCENICC program," Proc. SPIE **8383**, 838302 (2012).
[11] C. P. Chen, Z. Zhang, and X. Yang, "A head-mounted smart display device for augmented reality," CN Patent 201610075988.7 (2016).
[12] L. Zhou, C. P. Chen, Y. Wu, K. Wang, and Z. Zhang, "See-through near-eye displays for visual impairment," in *23rd International Display Workshops in conjunction with Asia Display* (2016), pp. 1114–1115.
[13] L. Zhou, C. P. Chen, Y. Wu, Z. Zhang, K. Wang, B. Yu, and Y. Li, "See-through near-eye displays enabling vision correction," Opt. Express **25**(3), 2130–2142 (2017).
[14] Y. Wu, C. P. Chen, L. Zhou, Y. Li, B. Yu, and H. Jin, "Near-eye display for vision correction with large FOV," in *SID Display Week* (2017), pp. 767–770.
[15] Y. Wu, C. P. Chen, L. Zhou, Y. Li, B. Yu, and H. Jin, "Design of see-through near-eye display for presbyopia," Opt. Express **25**(8), 8937–8949 (2017).
[16] C. P. Chen, Y. Wu, L. Zhou, Y. Li, B. Yu, and H. Jin, "A see-through near-eye display for presbyopia," in *17th International Meeting on Information Display* (2017), p. 209.
[17] C. P. Chen, L. Zhou, J. Ge, Y. Wu, L. Mi, Y. Wu, B. Yu, and Y. Li, "Design of retinal projection displays enabling vision correction," Opt. Express **25**(23), 28223–28235 (2017).
[18] L. Mi, W. Zhang, C. P. Chen, Y. Zhou, Y. Li, B. Yu, and N. Maitlo, "A retinal-projection-based near-eye display for virtual reality," Proc. SPIE **10676**, 106761C (2018).
[19] W. Zhang, Y. Wu, L. Mi, C. P. Chen, L. Zhong, B. Yu, Y. Li, and N. Maitlo, "Ultra-large field-of-view retinal projection display with vision correction," in *SID Display Week* (2018), pp. 1555–1558.
[20] Y. Wu, C. P. Chen, L. Mi, W. Zhang, J. Zhao, Y. Lu, W. Guo, B. Yu, Y. Li, and N. Maitlo, "Design of retinal-projection-based near-eye display with contact lens," Opt. Express **26**(9), 11553–11567 (2018).
[21] F. L. Pedrotti, L. M. Pedrotti, and L. S. Pedrotti, *Introduction to Optics 3rd Edition* (Addison-Wesley, 2006).
[22] M. Bass, C. DeCusatis, J. Enoch, V. Lakshminarayanan, G. Li, C. MacDonald, V. Mahajan, and E. V. Stryland, *Handbook of Optics 3rd Edition Volume III: Vision and Vision Optics* (McGraw-Hill Education, 2009).
[23] I. P. Howard, *Perceiving in Depth, Volume 1: Basic Mechanisms* (Oxford University, 2012).
[24] V. G. Chigrinov, V. M. Kozenkov, and H.-S. Kwok, *Photoalignment of Liquid Crystalline Materials: Physics and Applications* (Wiley, 2008).

[25] C. Chen, H. Li, Y. Zhang, C. Moon, W. Y. Kim, and C. G. Jhun, "Thin-film encapsulation for top-emitting organic light-emitting diode with inverted structure," Chin. Opt. Lett. **12**(2), 022301 (2014).
[26] J. Cao, J.-W. Xie, X. Wei, J. Zhou, C.-P. Chen, Z.-X. Wang, and C. Jhun, "Bright hybrid white light-emitting quantum dot device with direct charge injection into quantum dot," Chin. Phys. B **25**(12), 128502 (2016).
[27] P. Yeh and C. Gu, *Optics of Liquid Crystal Displays 2nd Edition* (Wiley, 2009).
[28] C. P. Chen, C. G. Jhun, T.-H. Yoon, and J. C. Kim, "Optimal design of omni-directional viewing angle switching panel," Opt. Express **15**(26), 17937–17947 (2007).
[29] R. E. Fischer, B. Tadic-Galeb, and P. R. Yoder, *Optical System Design 2nd Edition* (McGraw-Hill Education, 2008).
[30] I. Escudero-Sanz and R. Navarro, "Off-axis aberrations of a wide-angle schematic eye model," J. Opt. Soc. Am. A **16**(8), 1881–1891 (1999).
[31] Wikipedia, "Visual acuity," https://en.wikipedia.org/wiki/Visual_acuity.
[32] Wikipedia, "Nyquist–Shannon sampling theorem," https://en.wikipedia.org/wiki/Nyquist–Shannon_sampling_theorem.
[33] H. H. Hopkins, "The numerical evaluation of the frequency response of optical systems," Proc. Phys. Soc. B **70**(10), 1002–1005 (1957).
[34] Wikipedia, "Sunglasses," https://en.wikipedia.org/wiki/Sunglasses.